Towards Multiscale Digital Rocks: Application of a Sub-Resolution Production Model to a multiscale Sandstone

Rafael Salazar-Tio[1,*], *Andrew* Fager[1], *Guangyuan* Sun[1], *Bernd* Crouse[1], *Rui* Xu[1], *Brett* Wendt[2], and *Adam* Lewis[2]

[1]Dassault Systèmes, USA
[2]ConocoPhillips Alaska, USA

Abstract. Many digital rock methodologies use a direct simulation approach, where only resolved pores are accounted for. This approach limits the types of rocks that can be analyzed, excluding some types of carbonates, unconventionals, and complex sandstones from the digital rock analysis. This is due to the challenge for single scale imaging to capture the full range of relevant pore sizes present in multiscale rocks. In this paper, a physical model is presented, within the context of an established direct simulation approach, to predict the production of hydrocarbons including the contribution of sub-resolution pores. The direct simulation component of the model employs a multiphase lattice Boltzmann method to simulate multiphase fluid flow displacement in resolved pores. In the production model, the amount of hydrocarbons present in the sub-resolution pores is identified and a physical description of the production behavior is provided. This allows a relative permeability curve to be predicted for rocks where mobile hydrocarbons are present in pores smaller than the image resolution. This simplified model for the oil movement in the unresolved pore space is based on a physical interpretation of different regions marked by simulation resolution limits in a USBM wettability test curve. The proposed methodology is applied to high-resolution microCT images of a sandstone that contains pores at multiple scales, some resolved and some not resolved. To allow for benchmarking, experimental routine and special core analysis data was also obtained. Good agreement to experimental results is observed, specifically in absolute and relative permeability. The presented multiscale model has the potential to extend the classes of reservoir rocks eligible for digital rock analysis and paves the way for further advancements in the modelling of multiscale rocks, particularly unconventionals and carbonates.

1 Introduction

Reservoir characterization is a critical step in oil field exploration and production. Well logging analysis and petrophysical interpretation is usually supported by laboratory property measurements of physical core samples from the wells, such as porosity, saturations, capillary pressure (P_c), wettability, absolute permeability (K_0) and relative permeability (k_r). Laboratory core analysis can be a time consuming and costly process, and considering that most wells are not core sampled, the value extracted from the available core needs to be maximized, trying to make economically efficient use of these limited core samples [1]. Additionally, core analysis planning needs to consider also that conducting laboratory core analysis experiments sometimes leads to destructive impact on the rock samples. Relative permeability, in particular, is a difficult and time-consuming measurement that, depending on rock type, can take several weeks to a year to complete. With all these considerations, and with the advance of pore scale imaging techniques and computer power in the past decades, digital rock approaches have become more and more a promising technology to complement laboratory measurements [2-4].

Although digital rock technology is promising, there are still challenges when dealing with real applications involving less than ideal rocks, like heterogeneous lithologies or high clay content sandstones for instance. It is computationally costly to simulate a high-resolution large domain model that can resolve pore sizes over multiple orders of magnitude. On one hand, one would like to use a small field of view microCT imaging in order to capture pore-throat connections with a sufficient number of voxels. On the other hand, a large enough field of view is required in order to obtain a statistically representative elementary volume (REV) [5]. For instance in a clay-rich sandstone sample, we could find two different scale of pores sizes: inter granular pores with pore throat diameter around $\sim 10\mu m$scale and clay internal pores around $\sim 10nm$ scale. In order to achieve an REV model, microCT images need to be taken at a voxel resolution consistent with inter granular pores. At this scale clay internal pores fall below the voxel resolution and will be missed. In this case it is impossible to cover all pore scales in one digital rock analysis. There are several studies on the effect of unresolved pores and how to predict petrophysical properties, such as porosity, capillary pressure, absolute and relative permeabilities [6-10, 26-30] but none, to our knowledge, on how to predict relative permeability curves by using multiphase fluid flow from direct numerical simulation in high clay content sandstones, such as the case just described, leading to a model with significant amount of unresolved porosity.

This work investigate this case, a high clay content sandstone, by using an extension of current numerical digital rock workflows [11] to simulate fluid flow in rocks where a connected pore-space is resolved and unresolved pores do not provide a significant contribution to single phase flow,

* Corresponding author: Rafael.SalazarTio@3DS.com

however for multiphase flow can provide critical connectivity paths for the wetting phase and impact the overall behavior of k_r and P_c curves. The two samples used for this work are clay-rich reservoir sandstones; having nearly 50% porosity not resolved at typical microCT resolutions. In the remainder of this paper, we present the methodology and results of this application: A multi-mineral image segmentation is used to identify pores, grains and clay. A capillary pressure based physical model is presented to emulate oil movement in unresolved pore volumes. Porosity, k_0 and k_r are calculated in the total pore space and are compared well with SCAL laboratory measures available for these samples.

2 Method

The workflow contains three parts: pre-simulation work, simulation, and post-simulation work, which we describe in this section.

2.1. Pre-sim work

The main goal of the pre-sim workflow is to ensure that the microCT images for the selected mini-plug are suitable for digital rock analysis with a good resolution in a representative region. In the mini-plug sample preparation step, we consider sample location, sample size and microCT image resolution. Once the microCT image is done, it follows the image processing to obtain a 3D segmented image. The pore space is analyzed for connectivity and sufficient statistics. Finally, an estimation of total porosity is done.

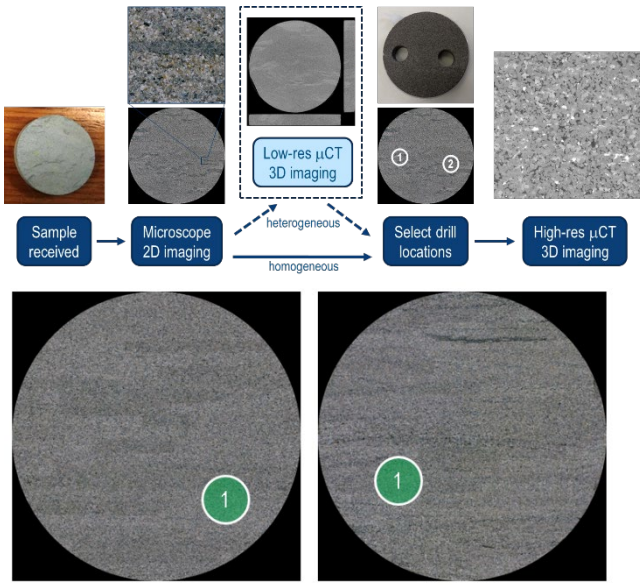

Fig. 1. Schematics of the pre-sim workflow (top). In the bottom, microscopy image of Rock A (left) and Rock B (right) with selected mini-plug locations.

2.1.1 Sample preparation

A schematic of the workflow for sample selection is shown in Figure 1. First, a large panoramic microscopy image is obtained of a polished surface of the available core sample, typically a few inches square at 4 $\mu m/voxel$ resolution. If heterogeneities are observed on the sample, an optional 3D microCT image can be taken of the core material at low resolution, typically 20 $\mu m/voxel$. These images are used in two ways: to select a suitable location for the mini-plug, and to get a rough estimation of grain size. A rule of thumb of 8-10 grains along the diameter of the mini-plug is used for the sample size [5], and the corresponding voxel-size is estimated by dividing the diameter by the number of voxels on the micro-CT camera. For the two samples in this paper, a 2.5 mm mini-plug diameter was estimated, which implies 1.0 $\mu m/voxel$ resolution given the 2500 $voxels$ in the microCT camera. We also show in Figure 1 the two-sample mini-plug locations used in this paper, Rock A, and Rock B.

2.1.2 Image processing

MicroCT images from mini-plugs typically require some image processing before they can be used successfully for segmentation. In the workflow, we first remove artefacts like beam hardening, rings, and intensity biases along the z-axis. The image noise level is reduced to our standard operational range by using a total variation filter, and grey-scale intensity is set to some default reference values. The main objective is to capture an accurate grey-scale interphase between pore-solid, in order to obtain the sub-resolution accuracy of the surface elements that are a defining feature of the LBM flow simulator utilized here.

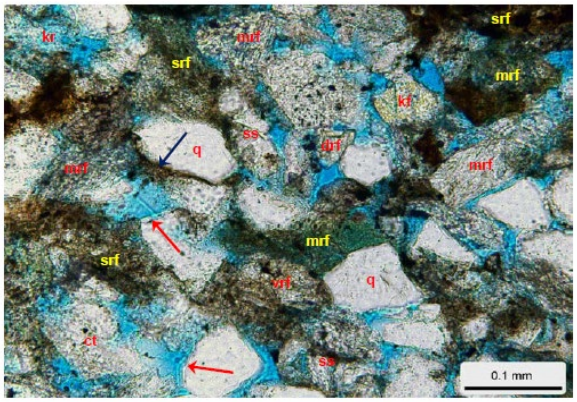

Fig. 2. Different mineral grains in Rock A, showing high clay content and metamorphic rock fragments. Quartz (q), metamorphic (mrf), shale (srf), chert (ct), dolostone (drf), siltstone (ss), volcanic (vrf), K-feldspar (kf), intergranular pores (blue).

In many cases, when complex mineralogy is present on the rock sample (see example in Figure 2), a multi-phase segmentation into different minerals is required. This is particularly important in cases with high clay content, with some partially dissolved grains of feldspars, or in cases with other unresolved porous structures, like in some carbonates. Some of these additional phases can contribute to the total porosity with pores of sizes smaller than the microCT resolution; therefore, an estimation of these fractions is necessary. A multi-mineral segmentation can also be used to model local wettability differences, in mix-wet multi-phase flow simulation scenarios.

An example of a multi-mineral segmentation is shown in Figure 3. This segmentation uses differences in grey values and intensity gradients to identify voxels along the solid-pore boundary and produce the resolved pore structure to be used

in the flow simulation. An additional segmentation for just the solid phase was done, mainly to estimate the porosity contribution from the clay regions, by using the differences in texture to separate minerals [25]. The mineral segmentation is then merged back to the solid-pore segmentation as shown in Figure 3 for Rock A, where we can identify the following volumetric fractions: 10.8% resolvable porosity (black), 12.2% microporous clay-type (yellow), grains 65% (light blue), heavy grains 9% (orange), bright grains 3% (dark blue).

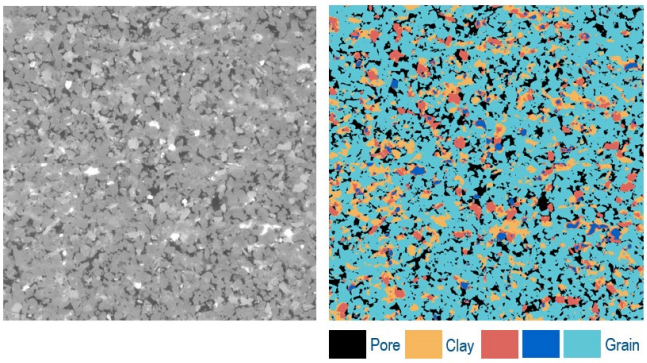

Fig. 3. Sample microCT image for Rock A and corresponding multi-mineral segmented image.

2.1.3 Pore Size Analysis

A pore space analysis (PSA) of the segmented resolvable pore phase is done as part of the pre-sim workflow in order to determine the voxel resolution and REV size for the final simulation model. Starting from calculating a coverable map for maximal inscribed sphere, a pore-size distribution can be computed as the distribution of pore volumes for each sphere radius. In this spherical approximation, the diameter of pores with a large aspect ratio can be underestimated. We also compute another similar volume distribution, but constrained by connectivity to an inlet surface for the model, and for decreasing values of the sphere radius. This connected accessible volume is used to estimate mercury intrusion capillary pressure (MICP) laboratory measurements by using the Young-Laplace relationship between capillary tube radius and capillary pressure, and to compute the critical radius for which the connectivity between inlet and outlet is established. A minimum of 3 $voxels$ is used to ensure accuracy in our multiphase flow simulation results, which corresponds to 3 μm for the microCT resolution used in this study. Finally, we estimate the convergence of the coefficient of variation (COV) of porosity and estimated permeability for different model sizes. COV is defined as the ratio of the standard deviation to the mean value. From the COV convergence analysis we determine what model size is statistically REV.

2.1.4 Estimation of total porosity

Given the physical limit imposed by the voxel-size in the microCT image, the fraction of the total porosity corresponding to pores smaller than the voxel-size cannot be directly measured from the image. However, using some considerations, an estimation of this unresolved porosity can be done. The first consideration follows the method described in [12] to estimate the non-clay unresolved porosity by fitting a Thomeer model for capillary pressure versus saturation as calculated using the PSA-MICP method described in the previous section. Using the resolvable porosity, voxel-size, critical radius and Thomeer G parameter, the non-clay unresolved porosity is estimated [12]. The second consideration involves including porosity contributions of some segmented phases from the image that could potentially have sub-resolution pores, like the clay phase shown in Figure 3 in yellow. Based on some clay mineral porosity studies [13, 14], we consider here an average of 50% contribution of the volume fraction corresponding to this segmented clay phase to complement the porosity estimation.

2.2 Simulation setup

The fluid flow numerical simulation approach used in this study is the Lattice Boltzmann method (LBM), which has been extensively used in digital rock applications, as a direct simulation approach for resolvable pore-scale events and capturing physical properties, such as residual oil on wettability dependence scenarios, capillary number effects and viscous fingering phenomena [11, 15-18]. The LBM is based on the kinetic equation, and represents a statistical description of the molecular behavior of fluid particles. The LBM can be used to simulate the dynamic behavior of fluid flow without directly solving the continuum fluid mechanics equations. Moreover, the LBM based fluid solvers are considered competitive alternatives to traditional Navier-Stokes PDE-based numerical methods [19, 20], particularly in applications involving complex geometries, like porous media flow in digital rock. The decoupling of streaming and collision steps also makes the LBM faster and more efficient in terms of computational efforts, at least compared to classical FE/FD-solvers.

The LBM solver used for this work is based on an extension of the multiphase Shan-Chen model (SC-LBM) [21]. Some of the recent extensions improve numerical stability and accuracy under the operating conditions required for digital rock workflows, such as low-resolution models and it includes the ability to deal with high viscosity ratios of the immiscible fluid phases [22-24]. In this multiphase LBM model, the fluid phase separation is the result of interaction forces between fluid components, while wettability is determined by interaction forces between fluid and pore walls [22]. Regarding the model geometry used in this LBM solver, in addition to the 3D volume elements corresponding to the voxels from the microCT scanned images, pore/solid surface elements, called surfels, are also used, which allow high fidelity representation of the pore/solid geometry interface with an effective sub voxel resolution accuracy [25, 26]. No slip boundary condition is applied between fluid and surfels.

2.2.1 Absolute permeability setup

Single-phase fluid flow can be simulated with the LBM solver in the resolved pore space. As per definition in Darcy's law, permeability is the linear proportionality ratio between flow rate and pressure gradient, which in this study is realized by a driving force applied in the flow direction, another option is to use pressure boundary conditions. The setup for

this simulation is used to simulate absolute permeability individually in each direction: x, y, z. A periodic boundary condition is applied in the flow direction, while no-flow boundary conditions are used in the directions transversal to the flow. The permeability is calculated using Darcy's Law when flow rate have converged.

2.2.2 Relative permeability setup

A similar setup as in single phase absolute permeability is used here, regarding the driving force applied in the flow direction, and no-flow boundary conditions in the directions transverse to flow, but using a multiphase LBM solver within a steady-state relative permeability displacement setup. In this setup, the water fractional flow starts from zero and keeps increasing until a predefined water saturation is reached. After both water and oil flow become stable, effective permeabilities are calculated and fractional flow increases again until the next water saturation.
Additional details for this method can be found in [11]. In multiphase fluid flow simulation, another parameter that needs to be defined is surface wettability by assigning a contact angle value to each surfel element. In our setup we consider a distribution of contact angles specified throughout the surface based on local contact by oil, as illustrated in Figure 4, where some pores/solid surface regions are considered more water wet and others more oil/neutral wet.

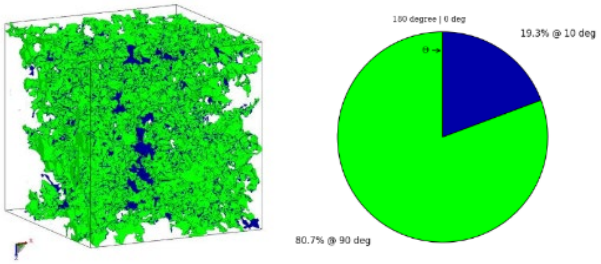

Fig. 4. Wettability setting for Steady-State Kr simulation.

The steady-state relative permeability displacement is conducted at constant capillary number N_c. The definition of capillary number used in this work is:

$$N_c = \frac{U_w * \mu_w + U_o * \mu_o}{IFT} \quad (1)$$

Where $U_{w,o}$ are the superficial velocities of water and oil, and $\mu_{w,o}$ are the dynamic viscosities of water and oil, while IFT is the interfacial tension between water and oil. In this work we use $N_c = 5 \times 10^{-7}$.

2.3 Post-sim and multi-scale model

2.3.1 Absolute permeability post-processing

Absolute permeability is calculated based on Darcy's law

$$K_{eff} = \frac{\nu * U}{g} \quad (2)$$

Where, ν is the kinematic viscosity, U is the volumetric superficial velocity from simulation, and g is the body force applied in the flow direction. The resulting absolute permeability value reflects only the flow contribution from the resolved pore space, while the contribution from the unresolved pore space is considered negligible in comparison. For the high clay content (above 10%) sandstones we are considering in this study, up to half of the pore space can be unresolved in the microCT images. However, as pointed out earlier, pores within clay can be several orders of magnitude smaller than inter granular resolved pores. Since permeability is proportional to pore-throat radius square, the flow contribution from clay pores is negligible when compared to the contribution from the resolvable pores, therefore the need for a multiscale procedure for absolute permeability in this case is less important [9].

2.3.2 Multi-scale post-processing for relative permeability

The resolved pore space relative permeability values for water and oil are calculated by Darcy's law at each converged saturation [11]. In this multiphase flow scenario, the fractional flow contribution from clay pores is also negligible when compared to the contribution from the resolvable pores, therefore we also consider here negligible the contributions of unresolved clay pores to the total flow, and use as a good approximation to the total flow the simulated flow only in the resolved pores, and the corresponding calculated relative permeability values K_r. However, the representation of $K_r(Sw_{sim})$ curves only considering saturations in the resolved pore space Sw_{sim} is incomplete and unsuitable for comparison with experimental results. The correct unknown curves are $K_r(Sw_{total})$ that consider saturations in the total pore space Sw_{total} instead. In this section, we explain how we can use a simplified model for the oil movement in the unresolved pore space and how we can rescale Sw_{sim} to Sw_{total} at each permeability calculation. This simplified model is based on a physical interpretation (capillary, wettability) of different regions marked by simulation resolution limits in a USBM wettability test curve.

One of the challenges in computing relative permeability curves in high clay content sandstones is that the unresolved pore space percentage can be larger than the initial water saturation percentage in experimental measurements. This indicates that there is oil in the unresolved pore space too. Such an amount of oil can be calculated from a USBM wettability test result. Figure 5 shows a schematic plot of a wettability test, illustrating the relationship between capillary pressure and water saturation. Let us consider the Young-Laplace equation to interpret the simulation resolution limits in this curve

$$\Delta P = \frac{IFT * 2cos\theta}{R} \quad (3)$$

Assuming a contact angle $\theta = 0$ near the end of USBM test and a minimum value for the pore radius R given by the microCT resolution, we can estimate a maximum limit for the capillary pressure ΔP that can be simulated in the resolved pore space of $IFT \times 2/resolution$, where IFT is the

interfacial surface tension between oil and water. Finer resolution values could resolve smaller pores and simulate a larger range of pressures, but at a higher computational cost.

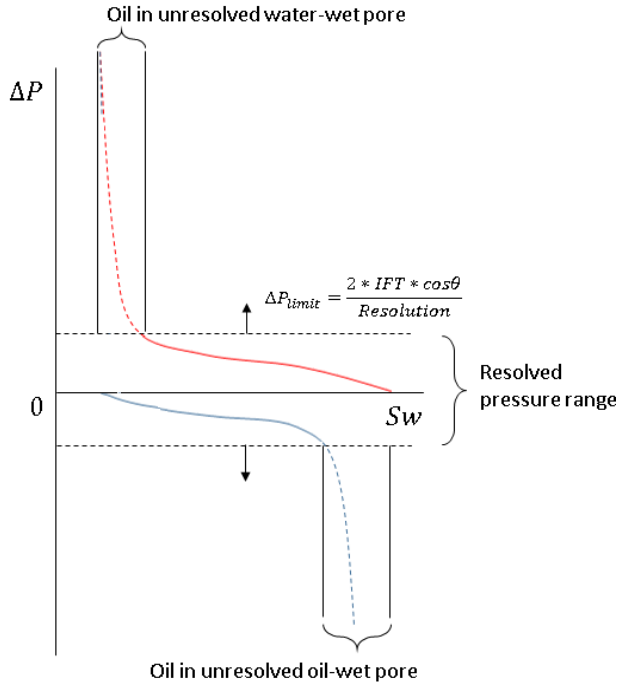

Fig. 5. Schematic plot illustrating the relationship between resolution, capillary pressure and amount of oil in unresolved water-wet and oil wet pore space.

The direct numerical simulation for relative permeability K_r can only be performed within the resolved pressure range shown in Figure 5. The red dash line in Figure 5 shows the amount of oil in the unresolved water-wet pore, which will be spontaneously imbibed before the beginning of the K_r simulation. The blue dash line shows the amount of oil in the unresolved oil-wet pore, which will not be displaced by water in the K_r simulation. For the rest of unresolved oil, we can assume a mix wet condition and model the oil displacement linearly during the K_r simulation. Figure 6 shows a schematic plot of how and when each part of the unresolved oil changes during the K_r simulation in the proposed model.

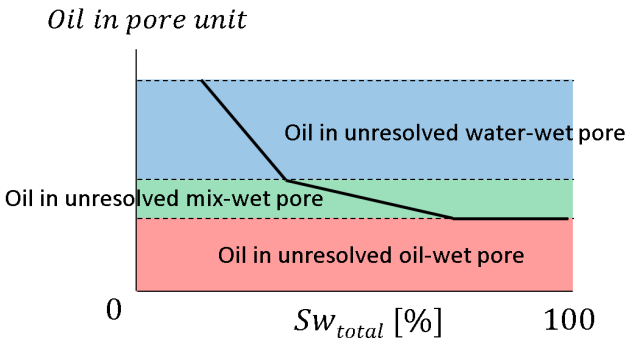

Fig. 6. Schematic plot of the amount of unresolved oil changes with saturation in the total pore space.

Since the proposed simplified model for the oil movement in the unresolved pore space is the main contribution in this paper, it is worthy to present next a summary of the steps to implement the model:

1. Provide an estimate of the total porosity and decompose it in resolvable and unresolvable porosities. Provide an estimate of the initial water saturation with respect to the total porosity.
2. Compute the amount of water/oil in the unresolvable pore space using the previous quantities.
3. Compute resolvable pressure simulation range using Equation (3); use it in the USBM wettability test curve to identify the regions marked in Figure 5, and estimate the allocation of oil in the unresolved pore space in 3 categories:
    a. water-wet: un-accessible pore volume above the max simulation pressure ΔP
    b. oil-wet: un-accessible pore volume below the min simulation pressure $-\Delta P$
    c. mix-wet: remaining pore volume to complete the total amount of oil in the unresolved pore space
4. Use a simple oil production model in the unresolved pore space (Figure 6):
    a. Oil in unresolved water-wet pore (blue): displaced before the simulation starts.
    b. Oil in unresolved oil-wet pore (red): never displaced by water.
    c. Oil in unresolved mix-wet pore (green): displaced from beginning to end of simulation using a linear rate.

The physical interpretation behind this model is based on simple relations between capillary displacements for different wettability and pore-size cases.

3 Results

We present in this section the results of the application of the methodology detailed in the previous sections to two reservoir rock samples: Rock A, and Rock B, both being tight sandstones with more than 10% clay content, some organic content, and other non-quartz minerals. As indicated in section 2.1.1 the microCT voxel-size used for both samples is 1 $\mu m/voxel$, and the REV estimated from the COV analysis described in section 2.1.3, about 800 voxels with a COV value around 25%. We select 1000^3 $voxels$ model size for porosity analysis and K_0 simulations, which are not too computationally expensive, but we just use 800^3 voxels for K_r simulations that are computationally more demanding.

3.1 Porosity

We apply the method described in section 2.1.4 to the segmented models of Rock A and Rock B. It is worth to notice that these rock samples have about half porosity unresolved below 1 µm, being from a digital rock perspective very challenging to characterize, however the resolved porosity is connected and the critical radius is properly resolved for flow simulations. The different values of porosity contributions are presented in Table 1.

Table 1. Porosity Calculation of Rock A, B

	Rock A	Rock B
Experimental	20.7%	19.6
Resolved	10.8%	10.2%
Resolved connected	10.2%	9.5%
Correct resolved connected	13.78%	12.37%
Clay image fraction	12.2%	13.9%
Clay porosity (assuming 50%)	6.1%	6.95%
Total porosity (calculated)	19.88%	19.32%

Experimental values of porosity are available for these two samples, and are compared with the image based total porosity estimation in Figure 7. The differences between experimental values and image estimations are within 5%, which is quite remarkable for samples with such significant unresolved porosity. Given the availability of the experimental porosities, for the sake of accuracy in the following simulations, we will be using the experimental values of total porosity; however, image porosity estimation can be used if experimental values were not available.

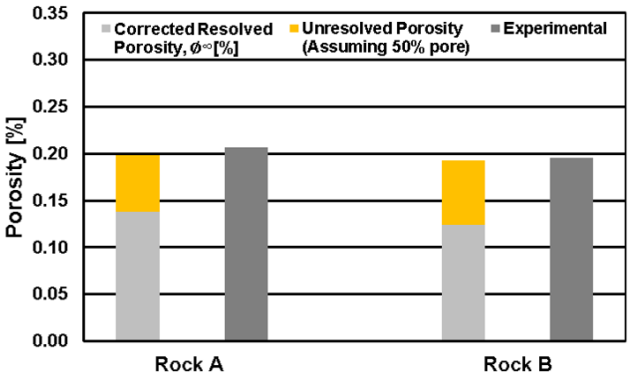

Fig. 7. Porosity Calculation of Rock A, and Rock B

3.2 Absolute Permeability

The results of the single-phase flow simulation setup described in section 2.2.1 in the resolved pore space are shown in Figure 8 where the flow velocity magnitude is represented in a color log scale. Flow in large connected channels contributes the most to the average flow speed and total permeability. Usually once the main flow paths in the pore space backbone are properly captured by the resolved porosity, the unresolved pore space contribution to flow seems to not be relevant anymore.

In Figure 9 we present the resolved pore space absolute permeability simulation results of Rock A and Rock B in x, y, z directions compared with the experimental values. The average simulated absolute permeability for Rock A is $21.2\ mD$ versus the experimental value $19.7\ mD$. The average simulated absolute permeability for Rock B is $16.0\ mD$ versus the experimental value $14.5\ mD$.

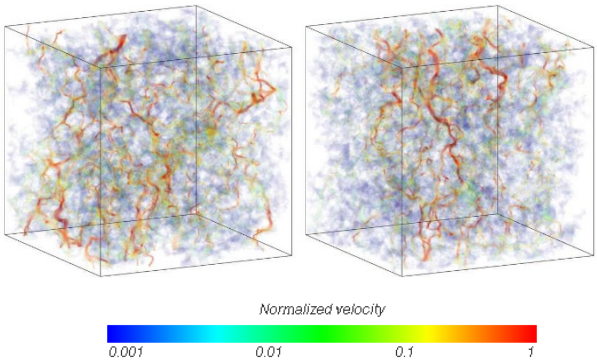

Fig. 8. Resolved pore space 1000^3 absolute permeability simulation in z-direction result of rock A (left) and rock B (right)

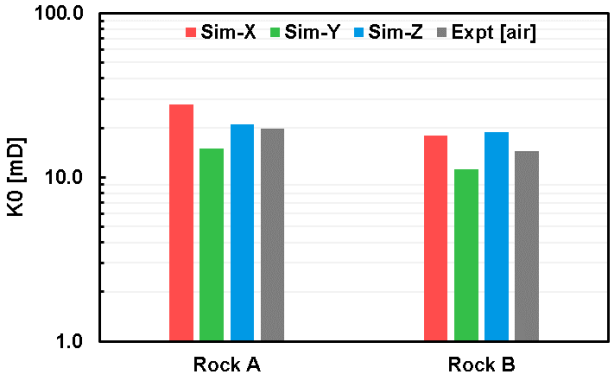

Fig. 9. Absolute permeability K_0 in x, y, z direction vs. experimental data

3.3 Relative Permeability

Following the methodology described in section 2.2.2, we setup the system wettability based on previous experience, knowledge of reservoir properties and USBM wettability lab measurements, as weakly water-wet to neutral-wet condition, by assigning a combination of 10 and 90 $degrees$ contact angles as shown in Figure 4. The initial water saturation in the simulation for the resolved pore space must be considered together with the unresolved initial water saturation, to be consistent with the experimental expected initial water saturation. In the simulation for the resolved pore space, we use an initial water saturation close to zero by assuming all water is in the unresolved pore space. This setup is consistent with the experimental initial water saturation for Rock A, which is 32.3%, considering that from the microCT images we can only resolve 52.2% of the total pore space, being 47.8% unresolved pore space missing in simulation. We use the same wettability and initial water setup for Rocks A and B.

In Figure 10 we illustrate the resolved pore space K_r simulation results for Rock A with two snapshots of oil and water distribution at early and late stages of displacement. At the bottom of Figure 10, we show the oil blobs color coded by blob size in log scale. Dark red represents the largest blob. Blue represents the smallest blob. At initial stages oil is well connected. At late stages when water saturation increases, oil blobs are more disconnected as more oil blobs are snapped off. The corresponding steady-state relative permeability

curve calculated from simulation in the resolved pore space $K_r(Sw_{sim})$ is shown in Figure 12 using green lines.

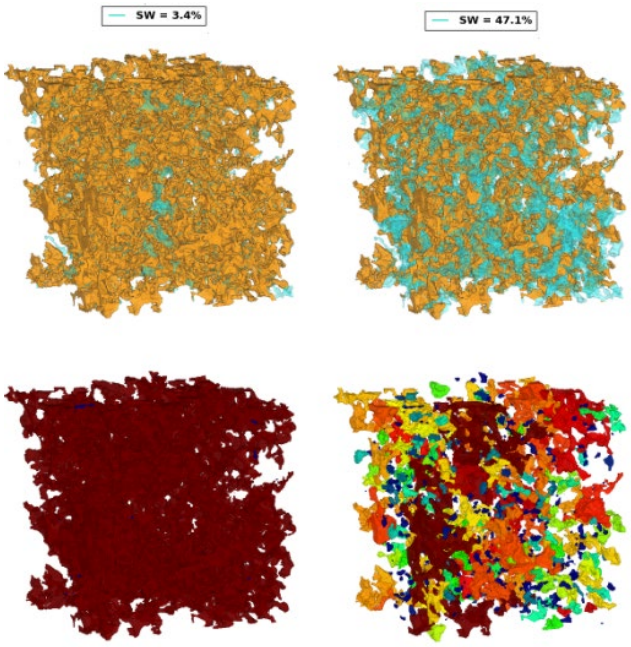

Fig. 10. Resolved pore space 800^3 voxels model for Rock A and steady-state relative permeability simulation results. Water (green)-oil (yellow) iso-surface visualisation (top). Oil blob iso-surface visualisation by blob size (dark red is largest blobs, blue is smallest blobs) (bottom).

We introduced an unresolved pore space oil production model in section 2.3.2 to describe how oil moves in the unresolved pore in order to calculate the correct $K_r(Sw_{total})$ curves for the total pore space by using USBM lab test results. In this study, the microCT resolution is 1.0 $\mu m/voxel$, IFT is 26 mN/m, so using Equation (3), the pressure limit is 7.54 psi. In Figure 11 we show the USBM test results for Rock A together with the estimated resolved pore space simulation pressure limits.

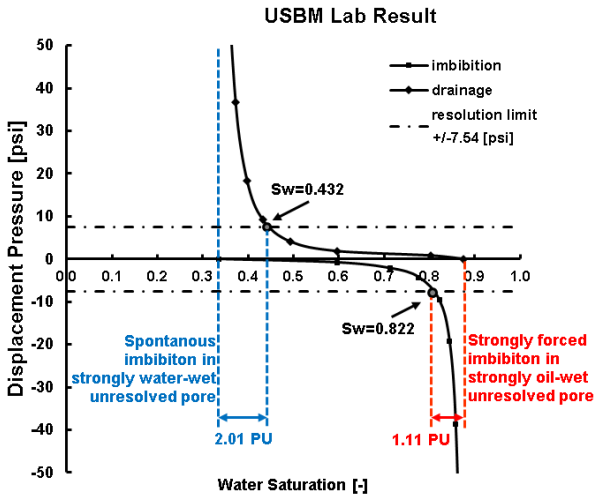

Fig. 11. USBM wettability test results for Rock A

The total porosity is 20.7% for Rock A, which corresponds to 20.7 Pore Unit (PU). Figure 11 shows that there is 2.01 PU of oil in unresolved water-wet pores and 1.11 PU of oil in unresolved oil-wet pores. Table 2 shows how the percentage of oil in neutral-wet unresolved pores is calculated, assuming $Sw_i = 0$ in the resolvable pore space simulation.

Table 2. Pore Unit calculation of initial oil in the unresolved pore space for Rock A: water-wet, neutral-wet and oil-wet.

	Percentage	Pore Unit
Total porosity (Lab)	20.7 %	20.7 PU
Resolved pore (Simulation pore space)	10.2 %	10.2 PU
Unresolved pore	10.5 %	10.5 PU
Connate water saturation in total pore space	32.2 %	6.67 PU
Assumed initial water in unresolved pore		6.67 PU
Derived initial oil in unresolved pore		3.83 PU
From USBM Result:		
Oil in water-wet unresolved pore		2.01 PU
Oil in oil-wet unresolved pore		1.11 PU
Oil in neutral-wet unresolved pore		0.71 PU

Following the linear production oil model illustrated in Figure 6, and using the input values from Table 2, we compute the red curves in Figure 12, that shows $K_r(Sw_{total})$ curves in total pore space after rescaling water saturation from resolved pore to total pore in sample Rock A, the black dots are lab test results. Overall, the simulation results and the experimental values match well in most of the K_r curves, which is remarkable considering that the resolved pore space in the simulation is only half of the total pore space. The mismatch of the first K_r point could be because the simulation computes the oil permeability at a lower oil saturation and a lower capillary pressure compared with lab, when oil has already been fully drained from the unresolved water-wet pore space. The direct numerical simulation reaches S_{OR} at the end of the solid line. An additional step is used to model the oil displacement through the unresolved pore space. The mismatch on the S_{OR} point could be due to such an effect. Another baseline for comparison can be obtained by compressing the green curve in the range 50%-100%, which corresponds to considering the half-unresolved porosity filled with unmovable water; this will overestimate the saturation crossing point.

Figure 13 shows $K_r(Sw_{sim})$ curves for Rock B simulated in the resolved pore space and $K_r(Sw_{total})$ in the total pore space by applying the same sub-resolution oil production model as per Rock A. Due to lack of lab results, a possible S_{OR} point from extended run was not done here for comparison. The simulated prediction for K_r is promising since Rock A and Rock B are similar rock types. Both have similar average grain size, belong to the same formation, have

similar mineralogy components, and clay content, the use of a similar oil production model is therefore justified.

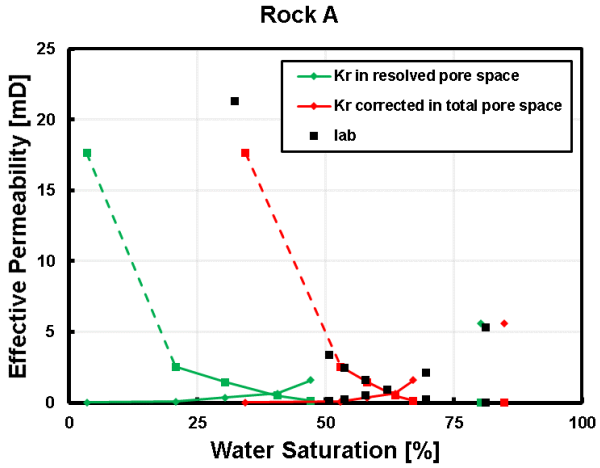

Fig. 12. $K_r(Sw_{sim})$ curves in the resolved pore space from direct simulation, $K_r(Sw_{total})$ curves in the total pore space using a production oil model, lab Kr results for Rock A.

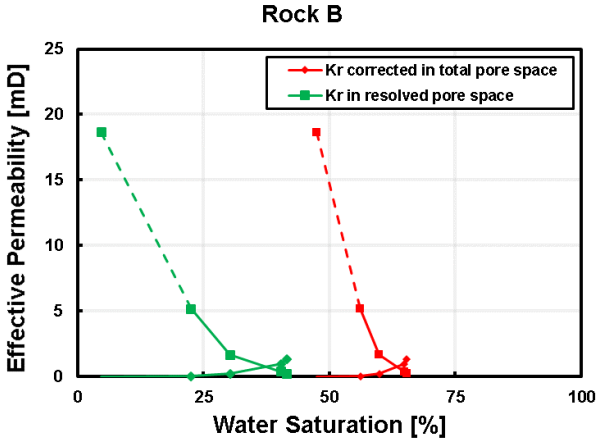

Fig. 13. $K_r(Sw_{sim})$ curves in the resolved pore space from direct simulation, $K_r(Sw_{total})$ curves in the total pore space using a production oil model, for Rock B.

4 Conclusions

A novel physics based sub-resolution oil production model is presented, which together with a digital rock workflow for multiphase fluid flow is applied to two clay rich sandstone reservoir rocks containing pores at two different scales. This simplified model is based on a physical interpretation (capillary, wettability) of different regions marked by simulation resolution limits in a USBM wettability test curve. For these high clay content sandstones, with half of the pore space below the microCT image resolution, the current workflow predicts porosities within 5%, absolute permeability within 10% and relative permeability K_r curves consistent with existing lab results. The current workflow demonstrate that is possible to use simplified models to extend the scope of application of digital rock technology to some challenging rock types, like high clay content sandstones, without having to explicitly simulate fluids movement in the unresolved pore regions using other multiscale multiphase flow methods such as [26-30]. In cases where the main percolating path is capture, but still a significant pore space fraction is unresolved, the method proposed in this paper could be computationally less expensive than full multiscale multiphase fluid flow methods [26-30].

References

1. J.J. Buckles, R. D. Hazlett, S. Chen, K. G. Eggert, D. W. Grunau, W. E. Soll, *Los Alamos Science*, **22**, 112-121, 1994.
2. S. Bakke, P. E. Øren, SPE 35479, *SPE Journal*, **2**, 136-149, 1997.
3. H. Andrä, N. Combaret, J. Dvorkin, E. Glatt, J. Han, M. Kabel, Y. Keehm, et al., *Computers & Geosciences*, **50**, 25–32, 2013.
4. H. Andrä, N. Combaret, J. Dvorkin, E. Glatt, J. Han, M. Kabel, Y. Keehm, et al., *Computers & Geosciences*, **50**, 33–43, 2013.
5. J. Bear, *Dover Publications Inc.*, 1988.
6. H. Long, C. Nardi, N. Idowu, A. Carnerup, M. A. Knackstedt, T. Varslot. SCA 2013-013, *Int. Symp. Soc. Core Analysts*, 2013.
7. S. Zhang, A. Byrnes, J. Howard, URTEC 2019-416, *Unconventional Resources Technology Conference*, Denver, Colorado, USA, 2019.
8. S. N. Apourvari, C. H. Arns, *Advances in Water Resources*, **95**, 161-175, 2016.
9. M. S. Jouini, S. Vega, A. A. Ratrout, *Geophysical Prospecting*, **63**, 405-421, 2014.
10. H. Zhang, P. Yuan, J. Wu, A. Mezzatesta, G. Jin, R. Satti, N. Koliha, J. Bautista, B. Crouse, and D. Freed, SPE 183883, *Middle East Oil and Gas Show & Conf.*, 2017
11. G. R. Jerauld, J. Fredrich, N. Lane, Q. Sheng, B. Crouse, D. M. Freed, A. Fager, and R. Xu, SPE 188688, *2017 SPE Abu Dhabi Int. Pet. Exhib. & Conf.,* Abu Dhabi, U.A.E., Nov. 13-16, 2017.
12. N. Saxena, A. Hows, R. Hofmann, J. Freeman, M. Appel, *Transp Porous Med* **129**, 403–412, May, 2019
13. P.H. Nadeau, A. Hurst, *Journal of Sedimentary Research*, **61**, 921-925, 1991.
14. A. Alansari, A. M. A. Salim, H. T. Janjuhah, A. H. B. A. Rahman, N. M. Fello, *Journal of Natural Gas Geoscience*, **4**, 139-150, 2019
15. B. Crouse, D. M. Freed, N. Koliha, G. Balasubramanian, R. Satti, D. Bale, and S. Zuklic, SCA 2016-058, *Int. Symp. Soc. Core Analysts*, Snow Mass, CO, USA. Aug. 2016.
16. R. Xu, B. Crouse, D. M. Freed, A. Fager, G. R. Jerauld, N. Lane, Q. Sheng, SCA 2018-066, *Int. Symp. Soc. Core Analysts,* Trondheim, Norway, Aug. 2018.
17. G. Sun, B. Crouse, D. M. Freed, R. Xu, J. Bautista, R. Zhang, H. Otomo, Y. Li, H. Chen, H. Fan, M. Dressler, *Fuentes, el reventón energético.* **16**, no. 2, 2018.
18. A. Fager, B. Crouse, G. Sun, R. Xu, D. M. Freed, SPE 195734, *2019 SPE Offshore Europe Conf. & Exhib.,* Aberdeen, UK, Sep. 2019

19. S. Chen, H. Chen, D. Martinez, and W. Mattheus, *Phys. Rev. Lett*., **67**, no. 27, 3776-3779, Dec. 1991.
20. H. Chen, S. Chen, W. Matthaeus, *Phys. Rev. A*, **45**, no. 8, R5339-R5342, Apr. 1992.
21. S. Chen and G. Doolen, *Annu. Rev. Fluid Mech.,* **30**, no. 1, 329-264, 1998.
22. H. Otomo, H. Fan, R. Hazlett, Y. Li, I. Staroselsky, R. Zhang, R., and H. Chen, H., *Comptes Rendus Mécanique*, **343**, 559 (2015).
23. H. Otomo, H. Fan, Y. Li, M. Dressler, I. Staroselsky, R. Zhang, and H. Chen, Jour. Comp. Sci., 17, 334 (2016).
24. H. Otomo, B. Crouse, M. Dressler, D.M. Freed, I. Staroselsky, R. Zhang, H. Chen, Computer Fluids, 172, 674 (2018)
25. I. Aranda-Carreras, V. Kaynig, C. Rueden, K.W. Eliceiri, J. Schindelin, A. Cardona, and H. Sebastian Seung, Bioinformatics, 33, 2424 (2017)
26. S. K. Masalmeh, X. Jing, S. Roth, C. Wang, H. Dong, M. Blunt, Society of Petroleum engineers SPE-177572-MS (2015)
27. L. C. Ruspini, G. Lindkvist, S. Bakke, L. Alberts, A. M. Carnerup, and P. E. Øren, Society of Petroleum Engineers SPE-180268-MS (2016)
28. O. Dinariev, N. Evseev, D. Klemin, SCA 2019-002, *Int. Symp. Soc. Core Analysts, 2019.*
29. M. Suhrer, X. Nie, J. Toelke, Proceedings of international petroleum technology conference, IPTC 20035 (2020)
30. A. Fager, H. Otomo, R. Salazar-Tio, G. Balasubramanian, B. Crouse, R. Zhang, H. Chen, J. Schembre-McCabe, *Int. Symp. Soc. Core Analysts, 2021*